Chapter 2

Theoretical Background

> Theory...
>
> "an extremely well-substantiated explanation of some aspects of the natural world that incorporates facts, laws, predictions, and tested hypotheses."
>
> Albert Einstein, 1916

As already mentioned in Chapter 1., the following sections will present in a compact form the basic theoretical principles on which the work for this thesis is based on. Particular emphasis will be put on presenting the samples used as well as on introducing the theory behind the experimental work performed.

2.1 The Cluster Beam

For the investigations performed during the work for this thesis, it has been considered that an effusive cluster beam will suffice. For this purpose, a cluster source with a thin walled orifice has been chosen (see Chapter 3.1.1. for a more detailed description of the source).
Due to the small dimensions of the orifice of area σ in comparison with the total area of the walls of the source the particles leaving the source will not perturb the thermal equilibrium of the particles inside. Denoting by $d\sigma$ the orifice area element, by dt the time unit and by $f(v)$ the speed distribution function in the source, one can write:

$$dN = n_0 \, f(v) \frac{d\omega}{4\pi} v \, \cos\theta \, d\sigma \, dt \, dv \tag{2.1}$$

where dN represents the number of particles leaving the area $d\sigma$ in the time interval dt into a solid angle $d\omega$ [14]. The velocity of the particles was assumed to be $v + dv$, while θ represents

the angle formed between the axis of $d\omega$ with respect to the normal to $d\sigma$.
Let us consider

$$v_w = \sqrt{\frac{2kT}{m}} \tag{2.2}$$

as being the most probable velocity in the system, with m being the molecular mass of the gas, T the thermodynamic temperature and k the Boltzmann constant ($k = 1.3806504(24) \times 10^{-23}$ J/K). The Maxwell-Boltzmann velocity distribution function will then be written:

$$f(x) = \frac{4}{\sqrt{\pi}} x^2 \, e^{-x^2} \, dx \tag{2.3}$$

where with x was denoted the ratio between v and v_w. Combining Eqs. 2.1 and 2.3, and denoting by $I(\theta, x)$ the particle flux into $d\omega$, we can therefore write:

$$\frac{dN}{dt}(\theta, x) = I(\theta, x)\, d\omega = \frac{n_0 \, d\sigma}{\sqrt{\pi^3}} v_w \, x^3 \, e^{-x^2} \, dx \, \cos\theta \, d\omega \tag{2.4}$$

Let $\nu_0 = \frac{n_0 v_w}{2\sqrt{\pi}}$ be the rate at which the particles enter the $d\sigma$ area.
Integrating over all velocities, Eq. 2.4 becomes:

$$I(\theta)\, d\omega = \nu_0 \, d\sigma \, \cos\theta \frac{d\omega}{\pi} \tag{2.5}$$

At large distances as compared to the dimension of the orifice, in front of the aperture (therefore, $\theta = 0$), one can calculate $I(0)$ by replacing $d\sigma$ through σ [15], which gives:

$$I(0) = \frac{\nu_0 \, \sigma}{\pi} \tag{2.6}$$

For practical reasons, however, Eq. 2.6 will be written:

$$I(0) = 1.4994 \times 10^{15} \, \frac{p_0 \, \sigma}{\sqrt{M \, T}} \quad \frac{molecules}{sr \, s} \tag{2.7}$$

where p_0 is the pressure expressed in bar inside the source, T and M are the absolute temperature and the molecular weight of the vapor, respectively and σ is expressed in m^2.

For the experiments performed during the work for this thesis, a cluster source with a circular orifice has been used (see Chapter 3.1.1 for more details on the cluster source) to create sulfur and selenium clusters.
The maximum intensity achievable for molecular flow with a circular aperture is obtained when the Knudsen conditions are fulfilled [16], meaning that $\sigma \approx \pi\Lambda^2$, with Λ being the mean free path

of the particles. Since $\Lambda \sim 1/p_0$ the maximum forward intensity will decrease linearly with the pressure in the source [14].

2.1.1 Sulfur

Sulfur, as an element can be found in the VI-th group of the periodic table of elements. This means that in the ground state, the sulfur atom has the electronic configuration $[Ne]3s^2\,3p^4$, two p-electrons being left unpaired. As the configuration of the outermost electronic shell resembles to the valence shell of the oxygen atom, similarities in the physical and chemical properties of the two elements are to be expected, such as, for instance, the energy levels of the excited states in S_2 and O_2 [17].

There are, however, also dissimilarities in the behavior and properties of the two elements, one of them being the structure of the stable form at room temperature. On one hand, at room temperature, oxygen's most stable form is the dimer O_2 which is gaseous. Sulfur, on the other hand is most stable at room temperature in the form of S_8 rings [18] which is a solid.

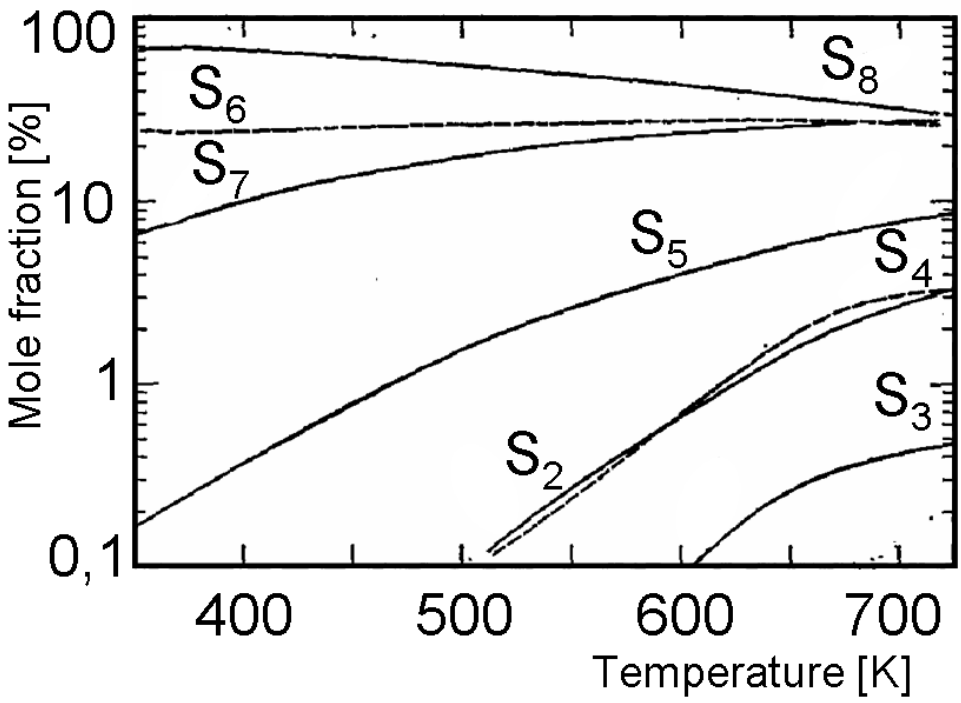

Fig. 2.1: Composition of sulfur vapor as a function of the temperature [19]

Such a major difference in the structure of the two elements has as a result major differences in what concerns the chemical properties of the two group VI elements. Responsible for this

are the low level unoccupied 3d-orbitals in sulfur [20] as well as the involvement of the 4s- and 3d-orbitals in the chemical bonding [21].

The only thermodynamically stable form of sulfur at room temperature is the orthorombic form [18, 22]. This form has a characteristic light-yellow color and consists of puckered S_8-rings [23]. $\alpha-$sulfur is insoluble in water, hardly soluble in alcohol and ether, but easily soluble in iodoform (CHI_3) and carbon disulfide (CS_2) [24].

For temperatures ranging between 300 K (room temperature) and 717.75 K (the boiling temperature of sulfur), sulfur is passing through many allotropic forms, characterized by variations in the viscosity and color, as previous studies have shown [25, 26, 27, 28]. It consists, as shown in Fig. 2.1, mainly of S_8 with small contributions of S_7 and S_6 [19]. However, as seen in Fig. 2.1, on increasing the temperature, the fraction of smaller sulfur clusters in the gas phase increases at the cost of the heavier aggregates.

On exceeding 2050 K, the sulfur dimers start dissociating, whereas for temperatures higher than 2450 K the dominant species is the atomic sulfur.

2.1.2 Selenium

The electronic configuration of the ground state of the selenium atom is resemblant to that of sulfur, being [Ar]$4s^2\,3d^{10}\,4p^4$. Similar to sulfur, selenium can be found in more than just one polymorph and allotrope forms, namely in some crystalline and amorphous red forms, in crystalline and vitreous black forms as well as in a crystalline gray form [24].

Selenium has six naturally occurring isotopes, namely ^{74}Se, ^{76}Se, ^{77}Se, ^{78}Se, ^{80}Se and ^{82}Se. These isotopes occur with approximate natural abundances of 0.88%, 8.95%, 7.65%, 23.51%, 49.62% and 9.39%, respectively [29]]. ^{77}Se, ^{78}Se, ^{80}Se, together with ^{80}Se also occur as fission products, out of which ^{79}Se has a halflife of 2.95×10^5 years, and ^{82}Se which has a very long half life (1.4×10^{20} years [30], decaying via double beta decay to ^{82}Kr) and for practical purposes can be considered to be stable. 23 other unstable isotopes have been characterized.

For the experiments performed during the work for this thesis, the gray form of selenium has been used, also known as *hexagonal selenium* [31]. This is the most thermodynamically stable and dense form of selenium and it has a melting point of 493.65 K [31]. It consists of long helical chains of selenium atoms, where the chirals have, in the same crystal, the same turning direction with 3 atoms per turn of the helix. The electrical conductivity of gray selenium is semiconducting-like, being strongly light sensitive (it exhibits photovoltaic properties).
Gray selenium is insoluble in water or alcohol, slightly soluble in carbon disulfide (CS_2) and easily soluble in ether.

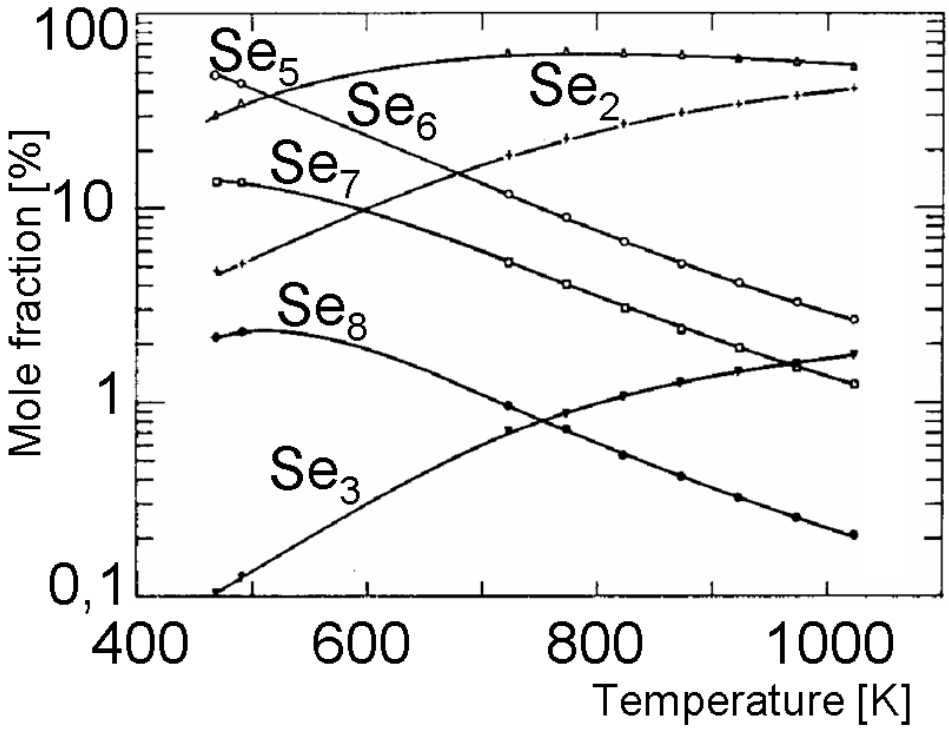

Fig. 2.2: Composition of selenium vapor as a function of the temperature [32]

For temperatures between 300 K (room temperature) and 958.15 K (the boiling temperature of selenium), the composition of selenium vapor changes dramatically. In the lower half of the temperature interval it consists, as shown in Fig. 2.2, mainly of Se_5 with a significant contribution from Se_6 [32]. Small amounts of Se_7, Se_2 and Se_8 have also bee observed [32, 33].
However, on increasing the temperature, the amount of Se_2 increases significantly at the cost of the heavier aggregates (Se_6, Se_7 and Se_8), such that by 1000 K the selenium vapor consists of over 90 % of Se_5 and Se_2 [32, 33] (see Fig. 2.2).

2.2 NEXAFS Spectroscopy

The X-ray absorption spectra are typically characterized by various spectral features in the proximity of the absorption edges. The X-ray absorption spectra can be divided into two distinct parts: the *NEXAFS* and the *EXAFS*, depending on the energy interval they investigate. The *EXAFS (Extended X-Ray Absorption Fine Structure)* is typically concerned with the energy region between 50 - 1000 eV above the absorption edge, whereas the *NEXAFS (Near Edge X-Ray Absorption Fine Structure)* spectroscopy is focused on the 0 - 50 eV energy interval above the X-ray absorption

edge [34]. In this energy interval one finds resonant structures that occur from the transition of inner-shell electrons into partially filled and empty states, reason for which the peak positions and the spectral line-shape in a *NEXAFS* spectrum depend on the nature of the unoccupied electronic state [35].

2.2.1 The Basic Principle

The basic phenomenon underlying NEXAFS is the absorption of an X-ray photon by an inner-shell electron of an atom and the subsequent emission of a photoelectron, as schematically depicted in Fig. 2.3. The core hole thus formed will be filled either via an Auger process or through the capture of a photoelectron from an outer-shell followed by the emission of a fluorescent photon. In NEXAFS one can measure either the initial photoelectron, the fluorescent photon, the Auger electron or an inelastically scattered photoelectron.

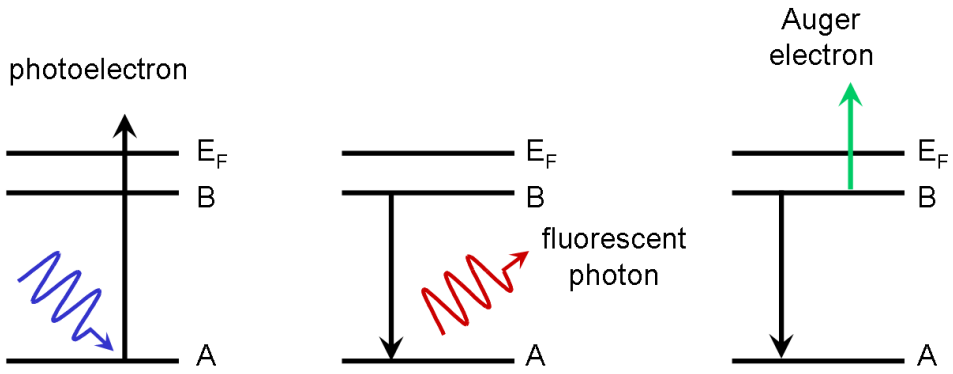

Fig. 2.3: Schematics of creation and filling of a core hole subsequent to the absorption of a X-ray photon

The effect of measuring fluorescent photons, Auger electrons, and directly emitted electrons is to sum over all possible final states of the photoelectrons, meaning that what NEXAFS measures is the total joint density of states of the initial core level with all final states, consistent with the conservation rules.

The predominance of one of these processes depends foremost on the atomic number of the excited atom. In the case of the *K*-shell this means that for high atomic numbers fluorescence is the prevalent process, whereas at low atomic numbers the Auger process is the dominant one. In the case of the *L*-shell, on the other hand, the Auger process is the prevailing one for $Z < 90$ [35].

For the soft X-rays case, the typical photon penetration depth is of the order of 100 nm. As a result, the emitted electrons passing through the material are transferring energy via inelastic

scattering to other electrons in the substance. This leads to the formation of cascades of electrons, or can activate vibrations.

If the path is too long, then the electrons (or the cascade of electrons) do not reach the surface, and, thus, they can not be detected. The mean free path of electrons has a broad minimum around a kinetic energy of about 70 eV (see Fig. 2.4). There the mean free path of the electron is less than 10 Å.This means that if we observe an electron with this kinetic energy which has left the solid without suffering an inelastic scattering event it must originate from the first few layers [36].

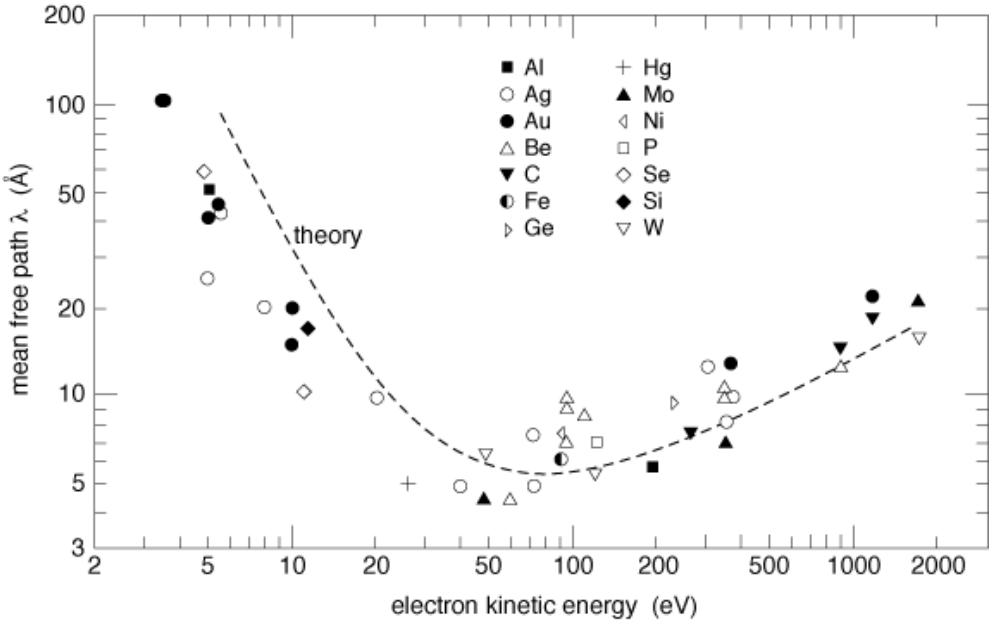

Fig. 2.4: The mean free path of the electrons in solid (the dashed curve is a theoretical result)[36]

The maximum detectable depth of a cascade of electrons is typically in the range from 5 to 15 nm, depending on the material, while the mean free path of a photoelectron and an Auger electron is smaller than 1 nm for the energy interval 50-600 eV [35].

2.2.2 Resonances at the Ionization Thresholds

In the NEXAFS spectroscopy of free and bound molecules transitions of inner-shell electrons into unoccupied antibonding molecular orbitals (MO's) are involved. The nature of the transition (i.e. a dipole transition from well defined initial and final states) implies that the excitation has to obey the dipole selection rule . This means that the change in the angular momentum quantum number should be $\Delta l = \pm 1$ between the initial and the final state.

The antibonding states are situated in the proximity of the absorption edge can be divided, for the *K*-edge into π^* and σ^* molecular orbitals .
The π^* orbitals are typically rather intense, due to the high overlap probability. The π^* orbitals are situated bellow the absorption edge , in contrast to the σ^* molecular orbitals, which can be found above the absorption edge, ofttimes in the form of broad features.

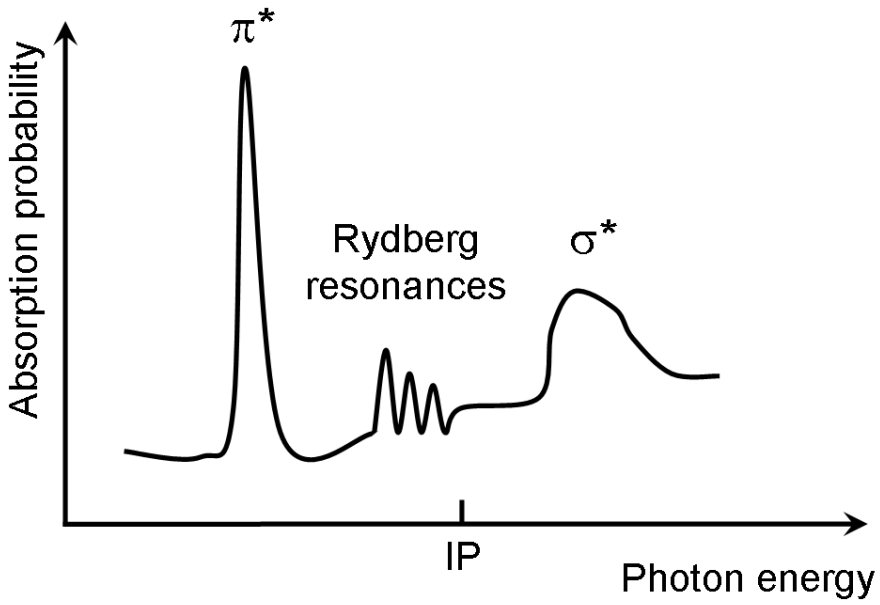

Fig. 2.5: K-edge NEXAFS spectrum of a diatomic molecule

The most noticeable feature in a NEXAFS spectrum is normally the π^* maximum (see Fig. 2.5). In the *K*-shell spectra of molecules with low *Z*, the π^*-resonance (the $1s \rightarrow \pi^*$ transition) is the resonance occurring at the lowest energy, typically bellow the ionization energy (usually denoted *IE*).
The reason for the resonance being below the IE is that the core hole (i.e. the missing electron in the core level) leads to an increase of the Coulomb potential which, in its turn, leads to a rearrangement of the outer orbital, translated in a red-shift (i.e. a shift towards lower energies) of the π^* resonance.

The intensity of the π^* resonance is an indicator of the oscillator strength (*f*) of the single electrons [35, 37]. The total oscillator strength of the transitions in an atom or a molecule is the sum of the oscillator strengths of all the single electrons of the atom or molecule, as described by:

$$\sum_n f_n + \int_{IP}^{\infty} \frac{df(E)}{dE} dE = N \tag{2.8}$$

Between the π^* resonance and the ionization potential one observes a series of maxima (see Fig. 2.6), occurring from transitions to Rydberg orbitals (Rydberg states) whose intensities are described by the first term in 2.8 [35].

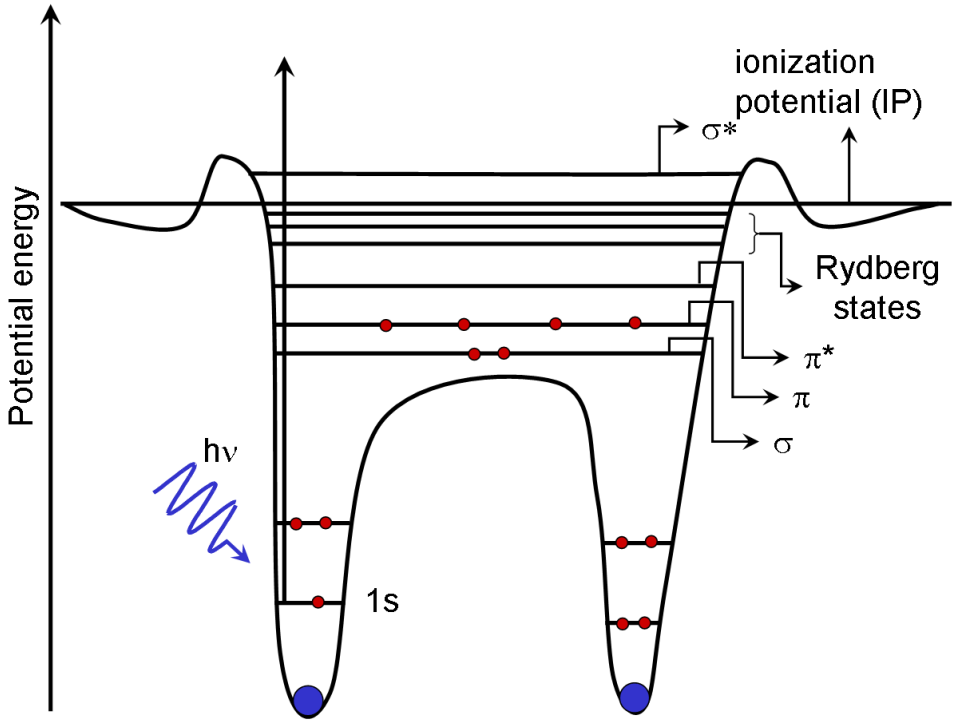

Fig. 2.6: Core-level excitation of a diatomic molecule, from the 1s level into unoccupied molecular orbitals

The number of empty molecular orbitals as well as their energy position is a characteristic property of the substance. Thus, the NEXAFS spectra below the ionization energy can be used as *fingerprints* in qualitative spectroscopy, for the identification of various molecular species.

In contrast to the energy region bellow the ionization energy, the energy interval above the IE is characterized by a broad resonance occurring from the σ^* molecular orbitals . The width of the σ^* resonance depends on the life time of the excited state and because the life time of the intermediary states is very short, the resonance will have a rather broad shape. The σ^* resonances are asymmetrical, exhibiting a maximum at low energies and a decay at high energies, shape which can be explained considering that usually, the higher the kinetic energy, the easier it is for the emitted electron to tunnel the potential barrier.

In the classical approach, the σ^* energy states are delimited by a potential barrier (see Fig. 2.6). Due to the resemblance of the shape of σ^* resonances to the shape of a potential barrier these resonances are sometimes referred to as *shape resonances*.
The σ^* resonances depend strongly on the vibrational state of a molecule, as the resonances

are dependent on the bond lengths in a molecule. Another important factor influencing the σ^* resonances is the atomic number (Z), meaning that for a given bond length, an increase of Z leads to a positioning of the resonances at higher energies [35].

Above the ionization energy in a NEXAFS spectrum one can find, apart from the σ^* resonances, also features arising from multi-electron effects , like the *shake-up* and the *shake-off* processes.
The *shake-up* process is an electron excitation process due to the sudden change of atomic potential, which can occur when an inner-shell electron is ionized via a photon or an atomic collision, or when an outer-shell electron is moved to an electronic inner-shell. Any kind of sudden change in the atomic potential causes the excitation of another outer-shell electron into a discrete unoccupied state or the continuum state .
When the electron is excited into a discrete energy level, the process is called *shake-up*, whereas when the electron makes a transition into a continuum level it is denominated as *shake-off*. The two process occur in a NEXAFS spectrum in the form of a sharp maximum (the *shake-up* process) or a step in the spectrum (the *shake-off* process).

2.3 Basics of Model Calculations

For performing theoretical calculations, one has to chose a chemical model for the system, formed from combining a theoretical method with a basis set, thus yielding an approximation of the Schrödinger equation. The time dependent Schrödinger equation is written:

$$H\,\Psi = i\hbar\,\frac{\partial \Psi}{\partial t} \tag{2.9}$$

where H represents the hamiltonian and Ψ stands for the wave function describing the system and $\hbar = \frac{h}{2\pi}$, with $h = 6.626069 \times 10^{-34}\ J \cdot s$ being the Planck constant.
If H is time independent and with r we denote the position vector, Eq. 2.9 becomes

$$\begin{aligned} H(r,t) &= H(r) \\ \Psi(r,t) &= \Psi(r)e^{\frac{-iEt}{\hbar}} \\ H(r)\Psi(r) &= E\Psi(r) \end{aligned} \tag{2.10}$$

Using the density functional theory (DFT) the ground state electronic energy can be completely determined by the electron density $\rho(r)$ [38], which can be connected to the singe particle wave function via:

$$\rho(r) = \sum_{occupied} |\Psi(r)|^2 \tag{2.11}$$

where the summation was done over all occupied electronic levels.
While the traditional *ab initio* methodology requires the resolution of the Schrödinger equation, DFT requires the minimization of the functional describing the energy of the system. In the DFT theory, according to Kohn and Sham [39] the total energy of a system $E_{DFT}[\rho]$ including electron correlation effects will be written:

$$E_{DFT}[\rho(r)] = T_S[\rho(r)] + E_{el}[\rho(r)] + E_{XC}[\rho(r)] \tag{2.12}$$

where $T_S[\rho(r)]$ is the kinetic energy part, $E_{el}[\rho(r)]$ is the electrostatic interaction energy between the elements of the system, which includes the electron-electron repulsion and the electron-nuclei attraction while $E_{XC}[\rho(r)]$ represents the exchange-correlation term.
It has been shown [38, 39] that the minimization of the energy is obtained for a set of orthogonal orbitals (Kohn-Sham orbitals), which can be determined either by numerical methods or by expansion into a set of basis functions.

For optimizing the geometry of selenium clusters DFT theoretical calculations have been performed by using the Gaussian98 [40] computer program. For the simulation of the near edge X-ray absorption spectra of selenium aggregates, the GSCF3 code has been employed [41, 42]. The GSCF3 code makes use of a combination of a "one-hamiltonian" method for solving the general self consistent field (SCF) equation and a "partial SCF" method for obtaining an initial guess of the orbitals [41].

For the calculations performed we have made use of various exchange functionals (theoretical methods) namely HF (Hartree-Fock [43]), B3LYP (which uses the non-local correlation that includes both non-local and local terms [44, 45, 46]), B3PW91 ([44, 47, 48]) and MP2 (Møller-Plesset second order perturbation theory [49])

Basis sets are mathematical descriptions of atomic orbitals in a system, which are used for performing theoretical calculations. Basis sets use linear combinations of Gaussian functions assigned to each atom within a molecule or cluster to approximate its orbitals. As, according to quantum mechanics, the electrons in a system have a finite and different from nil probability to be found anywhere in the system, the less constraints a basis set imposes on the position of the electrons, the more accurate is the results it delivers.

For the theoretical calculations presented in Chapter 4.2 the following basis sets have been employed: STO-3G, 6-31G, 6-311G,3-21G and LANL2DZ.

The STO-3G is a minimal basis in which each occupied atomic orbital (Slater-type orbital [50]) is approximated by three Gaussian functions [51, 52].

The 6-31G basis set represents a split valence basis set in which the core orbitals are described by a contraction of six primitive Gaussian type orbitals (PGTO), while the valence orbitals are

described by additional four PGTO's: three of them describe the inner part and one describes the outer part of the valence orbitals [53].

The 6-311G set is a triple split valence basis set in which the core orbitals are described similar to the 6-31G set, while the description of the valence orbitals is split into three functionals formed respectively from three, one and one primitive Gaussian type orbitals [54].

The 3-21G set describes the orbitals in a similar manner to 6-31G, just that the number of PGTO's used is smaller, and thus, the set is more inaccurate [55].

The LANL2DZ (Los Alamos National Laboratory 2Double-Zeta) basis set uses a relativistic effective core potential (ECP) combination, derived from numerical Hartree-Fock wave functions. These have been generated to be used in theoretical calculations on molecules and clusters where the outermost core orbitals and the valence orbitals have to be treated in an explicit way simultaneously [56, 57, 58].

2.4 The Dynamics of Fragmentation

Subsequent to inner-shell excitation of cluster, relaxation processes (e.g. Auger decay) can lead to the formation of multiply charged clusters. Due to the Coulomb repulsion between the electric charges, the clusters can brake apart into charged fragment ions, electrons and, sometimes, neutral particles, as suggested by the following mechanism:

$$ABC + h\nu \rightarrow (ABC)^{n+} + ne^{-} \rightarrow A^{m+} + B^{(n-m)+} + C \tag{2.13}$$

The charged particles can be detected, for example, by making use of a time-of-flight mass spectrometer [59].

A powerful approach for studying the fragmentation is the photoelectron-photoion-photoion-coincidence (PEPIPICO) spectroscopy technique. This approach requires the use of an electron resulting from the fission process for starting the measurement, in order to provide the $t = 0$ time, as, due to their velocities, they arrive virtually instantaneously at the electron detector. As stop signals of the measurements one will use the ions emitted in the dissociation of the parent ion. Plotting in 2D the flight time of the second ion (t_2) versus the arrival time of the first ion on the ion detector (t_1) one obtains a set of ion-ion coincidence signals.

From the analysis of the time of flight distribution of the ions recorded in coincidence one can draw important conclusions regarding the dynamics of the fragmentation process involved in the occurrence of the cation pairs. The fragmentation of clusters can take place in one or more steps, each different process being visible through a different correlation plot pattern. Thus it is possible

to differentiate between two-, three- or four-body fragmentation processes.
The widths of the coincidence signals in a PEPIPICO spectrum is directly proportional to the kinetic energy release (KER) of the fragmentation processes. Assuming a simple approach of a Coulomb explosion for explaining the fission mechanism, one can determine from the kinetic energy release the charge separation distance (CSD). The CSD is the distance which separates the two charges in the doubly charged parent ion, and is calculated according to Coulomb's law as follows:

$$CSD = \frac{1}{4\pi\varepsilon_0\varepsilon_r} \times \frac{q_1 q_2}{KER} \tag{2.14}$$

where q_1 and q_2 are the two electrical charges, ε_0 is the electrical permittivity of the free space and ε_r is the electrical permittivity of the medium in which the two charges are situated relative to the free space.
The prefactor ($\frac{1}{4\pi\varepsilon_0}$), termed the electrostatic constant (commonly denoted by k_C), assumes the use of SI units and is included to ensure that a pair of one Coulomb charges, separated by one meter in vacuum, each experience a force of one newton, and has the magnitude given by:

$$k_C = \frac{1}{4\pi\varepsilon_0} \approx 8.988 \times 10^9 [Nm^2C^{-2}] \tag{2.15}$$

2.4.1 Two-body Processes

The simplest scenario of a fragmentation mechanism is the two-body process. This is a process in which as a result of the fission step two fragment ions are obtained, as described by the following process for the fragmentation of a doubly charged ion:

$$AB + h\nu \rightarrow (AB)^{2+} + 2e^- \rightarrow A^+ + B^+ \tag{2.16}$$

A schematics of the two-body dissociation mechanism and of the ideal PEPIPICO signal shape is depicted in Fig. 2.7 for the case where the two ions have the same mass and the same charge. In Fig. 2.7 it was assumed that ion A^+ is the ion with the shorter time of flight and that ion B^+ is the ion flying longer. As a result of the Coulomb explosion of the parent ion, due to kinetic momentum conservation, the two ions must have kinetic momenta of the same vector direction and magnitude (denoted in Fig. 2.7 with p) and opposite direction.

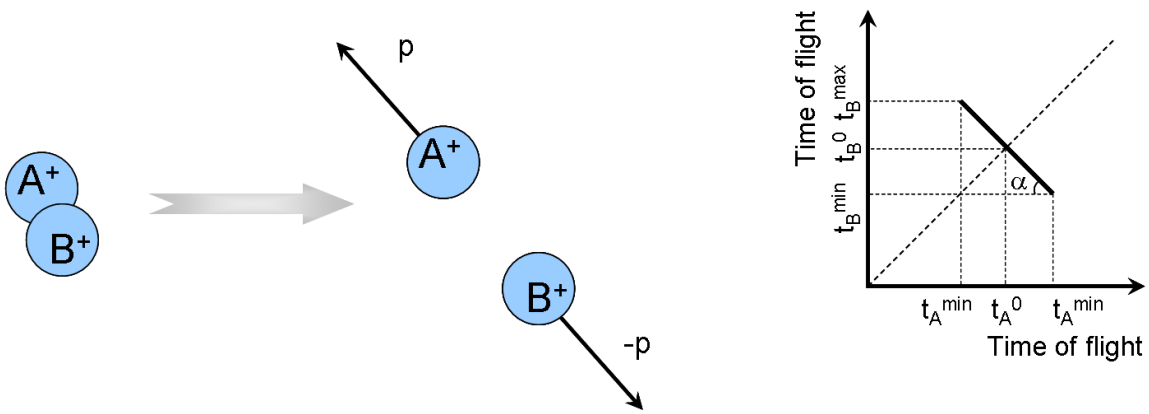

Fig. 2.7: Schematics of a two-body dissociation, together with an ideal PEPIPICO signal shape

In our experiments we made use of a Wiley-McLaren time-of-flight mass spectrometer [59]. In order to achieve sufficient spread in the flight time of the recorded ions so that a reasonable determination of the KER accompanying charge separation is obtained [60, 61, 62, 63, 64, 65, 66], one will choose to work with low extraction field conditions. Due to this constraint, one detects mainly a small portion of the ions, namely the ones flying along the axis of the spectrometer. Therefore, with such an experimental setup one can determine mostly the kinetic momentum component along the axis of the spectrometer (the z-axis).

Considering that after the ionization process, the doubly charged ion can rotate around any direction (x, y or z), the two fragments can be emitted in any direction. This means that the times of flight of the two ions can take any value between t_A^{min} and t_A^{max} and t_B^{min} and t_B^{max}, respectively, where t_A^{min} (t_B^{min}) is recorded when ion A^+ (B^+, respectively) is flying parallel to the z axis and directed to the detector, while t_A^{max} and t_B^{max} are obtained when the ions are flying along the z-axis, but directed away from the ion channel-plate detector. As the process is symmetrical, a t_B *vs* t_A plot will be a straight line with a slope of *-1* of length l, where the magnitude of l is given by:

$$l = \sqrt{2}\Delta t \tag{2.17}$$

where by Δt we understand the spread in the time-of-flight of the ions A^+ and B^+, namely:

$$\Delta t = t^{max} - t^{min} \tag{2.18}$$

Using the result from Eq. 2.17, and knowing the electric force ($\vec{F}$) acting upon the ions in the spectrometer, one can determine the kinetic momenta of the ions:

$$p = \frac{l\vec{F}}{2\sqrt{2}} \tag{2.19}$$

which we can further on use in order to calculate the kinetic energy of the dissociation:

$$KER = \frac{p^2}{2\mu_{A,B}} \tag{2.20}$$

where

$$\mu_{A,B} = \frac{m_A m_B}{m_A + m_B} \tag{2.21}$$

is the reduced mass of the system. Introducing the result from Eq. 2.20 into Eq. 2.14 one can thus deduce the charge separation distance in the parent ion.

2.4.2 Three-body Processes

Three-body processes are processes in which, apart from the two charged fragments detected by the ion detector, the emission of a neutral one can also be proved, as suggested bellow for the dissociation of a doubly charged cation:

$$ABC + h\nu \rightarrow (ABC)^{2+} + 2e^- \rightarrow A^+ + B^+ + C \tag{2.22}$$

Based on the sequence in which the charge separation and the emission of the neutral take place, one can distinguish three different process types [60, 66]: (a) concerted three-body dissociation, (b) deferred charge separation and (c) secondary decay.

(a) Concerted three-body dissociation

Such a process involves the simultaneous break-up of the bonds holding together the three moieties A, B and C after the double ionization, as suggested bellow:

$$ABC^{2+} \rightarrow A^+ + B^+ + C \tag{2.23}$$

As a result, the kinetic momenta distribution is not unique, as pointed out by Eland [60], as the separation of the particles can be prevented through collisions between fragments.

In consequence, the expected slope of the process described as a general case by Eq. 2.22 can take any value between -1 and $\frac{m_A}{m_A+m_C}$ and -1 and $\frac{m_B}{m_B+m_C}$, respectively, depending on if we are dealing with a collision between fragments A^+ and C or B^+ and C.
A collision between A^+ and B^+ is highly unlikely, due to the Coulomb repulsion forces.

(b) Deferred charge separation

The deferred charge separation mechanism is a two step process in which, prior to charge separation, the doubly charged ion is releasing a neutral, as described in Fig. 2.8 and in the following mechanism:

$$ABC^{2+} \rightarrow AB^{2+} + C$$
$$AB^{2+} \rightarrow A^+ + B^+ \tag{2.24}$$

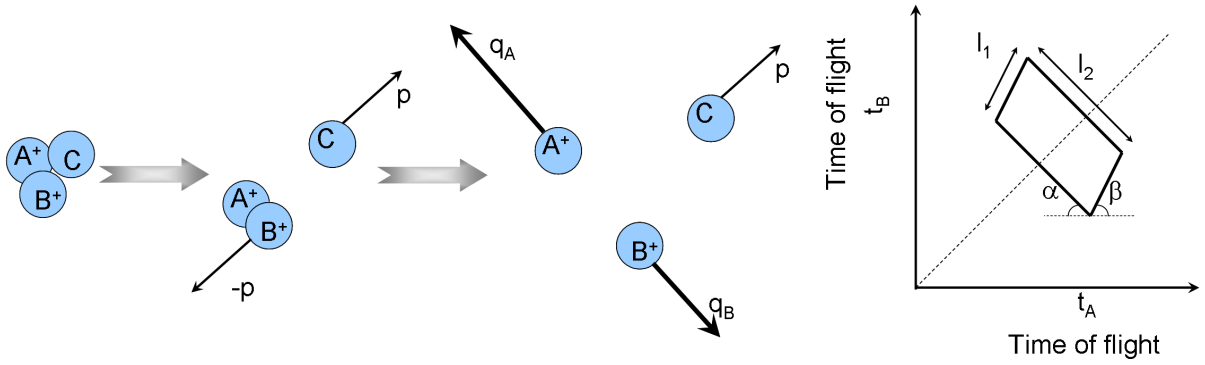

Fig. 2.8: Schematics of a deferred charge separation mechanism, together with an ideal PEPIPICO signal shape

Let us denote by p the kinetic momentum of the neutral C after the first step of the dissociation and by U_1 the kinetic energy release of this process. We can, therefore deduce that:

$$p^2 = \frac{2U_1}{\mu_{AB,C}} \tag{2.25}$$

where by $\mu_{AB,C}$ we have denoted the reduced mass of the ensemble formed by AB^{2+} and C, and has the magnitude as defined by Eq. 2.21.
If we denote by q the kinetic momentum of A^+ in the AB^{2+} frame after the charge separation step, due to kinetic momentum conservation, the resultant kinetic momentum of the two ion, q_A and q_B, are defined as follows:

$$\overrightarrow{q_A} = \overrightarrow{q} + \frac{m_A}{m_A + m_A}\overrightarrow{p} \tag{2.26}$$

and

$$\overrightarrow{q_B} = \overrightarrow{q} + \frac{m_B}{m_A + m_A}\overrightarrow{p} \tag{2.27}$$

respectively, where by U_2 one understands the kinetic energy release of the charge separation step. Thus, combining Eq. 2.25, Eq. 2.26 and Eq. 2.27 we obtain:

$$q_A = \sqrt{2U_2\mu_{A,B}} + \frac{m_A}{m_A + m_A}p \tag{2.28}$$

and

$$q_B = \sqrt{2U_2\mu_{A,B}} + \frac{m_B}{m_A + m_B}p \tag{2.29}$$

The t_B *vs* t_A correlation plot will, therefore be described by a parallelogram whose long edge has a slope of -1 ($m = \tan\alpha = -1$) (as the charge separation process is a two-body process) and the length defined by:

$$l_2 = \frac{2q\sqrt{2}}{F} \tag{2.30}$$

with F being the electric force acting upon the ions in the spectrometer.
The slope of the short edges of the parallelogram, denominated "the secondary slope", corresponds to the kinetic energy release of the second dissociation. It is defined [67] by $b = \tan\beta = -m_A/m_B$ whereas the lengths of the short edges of the parallelogram are defined as follows:

$$l_1 = \frac{2p}{F}\frac{\sqrt{{m_A}^2{m_B}^2}}{m_A + m_B} \tag{2.31}$$

(c) Secondary decay

The secondary decay mechanism describes a two step fragmentation mechanism in which one of the ions formed in the charge separation step releases a neutral, as suggested in Fig. 2.9 and in the following process:

$$ABC^{2+} \rightarrow A^+ + BC^+$$

$$BC^+ \rightarrow B^+ + C \tag{2.32}$$

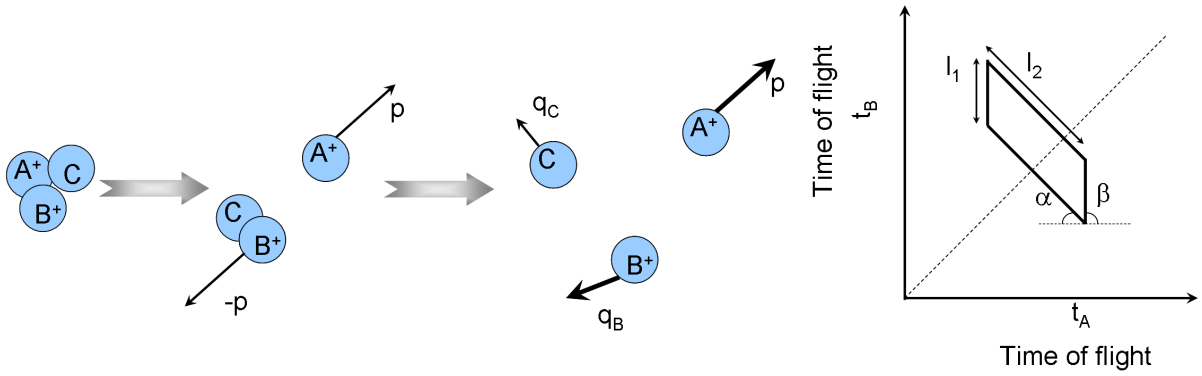

Fig. 2.9: Schematics of a secondary decay mechanism, together with an ideal PEPIPICO signal shape

In a similar manor like the deferred charge separation case it can be shown that the momenta of the ions after the two steps of the dissociation are:

$$q_A = p = \sqrt{2U_1\mu_{A,BC}} \tag{2.33}$$

and

$$q_B = \sqrt{2U_2\mu_{B,C}} + \frac{m_B}{m_B + m_C}p \tag{2.34}$$

respectively, where q_A, q_B are the kinetic momenta of the A^+ and B^+ ions and by $\mu_{A,BC}$ and $\mu_{B,C}$ we understand the reduced mass of the respective system of moieties.

The expected PEPIPICO plot in this case will be a parallelogram with two edges horizontal or vertical, depending on whether the moiety releasing the neutral is the lighter one or the heavier one [66]. The other two edges of the parallelogram have a slope m defined as follows:

$$m = \tan\alpha = -\frac{m_B}{m_B + m_C} \tag{2.35}$$

The lengths of the edges of the parallelogram can be determined to be:

$$l = \frac{2q}{F} \tag{2.36}$$

and

$$L = \frac{2p}{F}\frac{\sqrt{(m_B + m_C)^2 + m_C{}^2}}{m_B + m_C} \tag{2.37}$$

where through q we understand the kinetic momentum of the B^+ and C particles in the second step of the dissociation in the B^+C frame.

Making use of the Eqs. 2.33, 2.34, 2.36 and 2.37 one can easily deduce the kinetic energy release of the two steps of the dissociation.

2.4.3 Four-body Processes

A four-body ion pair process is a process in which a doubly charged parent ion $ABCD^{2+}$ breaks up into A and B^+ and C^+ and D, as described by the following mechanism:

$$ABCD + h\nu \rightarrow (ABCD)^{2+} + 2e^- \rightarrow A + B^+ + C^+ + D \tag{2.38}$$

Four-body ion processes can be arranged into three classes [66]: (a) concerted four-body dissociations, (b) deferred charge separations and (c) secondary decays.

(a) Concerted four-body dissociation

The concerted four-body dissociation mechanism assumes an instantaneous break-up of all the chemical bonds holing the four moieties together. Such a process is unlikely, but it can be that the bond breaking happens so fast that the different steps can not be experimentally distinguished from each other.

(b) Deferred charge separation

As the deferred charge separation mechanism involves releases of neutrals prior to charge separation, as described by:

$$\begin{aligned} ABCD^{2+} &\rightarrow ABC^{2+} + D \\ ABC^{2+} &\rightarrow AB^{2+} + C \\ AB^{2+} &\rightarrow A^+ + B^+ \end{aligned} \tag{2.39}$$

this process cannot be distinguished from a three-body charge separation in which the parent ion $ABCD^{2+}$ would lose in the first step the CD moiety. As a result, the expected PEPIPICO shape will be a parallelogram which has the slope of the long edge $m = -1$.

(c) Secondary decays

As already mentioned in the previous subchapter, secondary decay processes imply the release of neutrals after charge separation took place. We can therefore distinguish between two different secondary decay paths [66]: (I) the secondary decay after a deferred charge separation and (II) the secondary decay in competition.

(I) Secondary decay after a deferred charge separation

This process is described by the following path:

$$\begin{aligned} ABCD^{2+} &\rightarrow ABC^{2+} + D \\ ABC^{2+} &\rightarrow A^{+} + BC^{+} \\ BC^{+} &\rightarrow B^{+} + C \end{aligned} \tag{2.40}$$

This mechanism, however, cannot be distinguished from a three-body secondary decay process, as the first emission of the neutral D only provides the doubly charged ABC^{2+} ion with a non-zero kinetic momentum. As this emission can take place in any direction, this results in an isotropic distribution of the kinetic momentum of ABC^{2+}. Therefore, it is considered that the treatment of the data has been in sufficient detail in Chapter 2.4.2 and will not be discussed further.

(II) Secondary decay in competition

This path involves that both singly charged ions resulting from the charge separation step suffer a subsequent decay, as describe by Fig. 2.10 and by the following mechanism:

$$\begin{aligned} ABCD^{2+} &\rightarrow AB^{+} + CD^{+} \\ AB^{+} &\rightarrow A + B^{+} \\ CD^{+} &\rightarrow C^{+} + D \end{aligned} \tag{2.41}$$

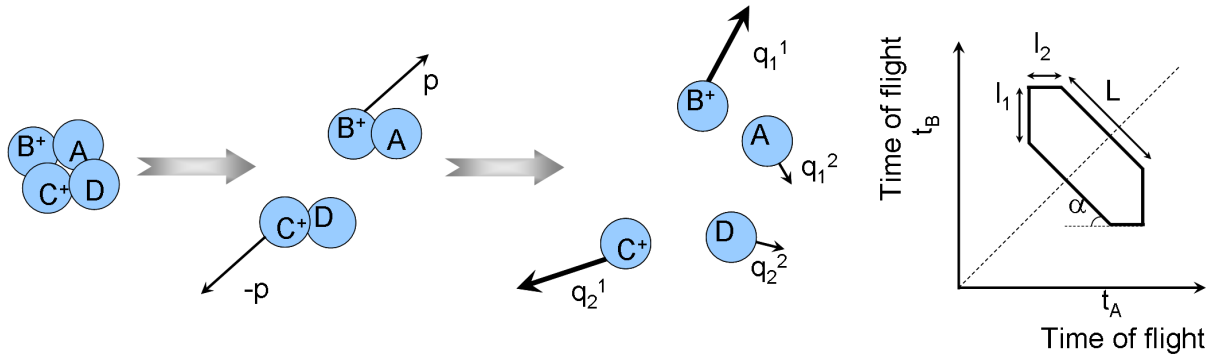

Fig. 2.10: Schematics of a secondary decay in competition mechanism, together with an ideal PEPIPICO signal shape

Such a mechanism will lead to the formation of a coincidence signal of hexagonal shape, if the kinetic momenta of the recorded ions are far smaller than the kinetic momentum of the cations after the charge separation step.

The hexagonal pattern will have two horizontal and two vertical edges determined by the kinetic momenta of the neutral emission processes and two oblique edges with a slope

$$m = -\frac{m_B}{m_A + m_B}\frac{m_C + m_D}{m_C} \tag{2.42}$$

or

$$m = -\frac{m_C}{m_C + m_D}\frac{m_A + m_B}{m_B} \tag{2.43}$$

depending on whether B^+ or C^+ is the heavier of the correlated cations. The length L of the inclined edge is then determined by:

$$L = \frac{2p}{F}\sqrt{\frac{m_C}{m_C + m_D}^2 + \frac{m_B}{m_A + m_B}^2} \tag{2.44}$$

where p is the kinetic momentum of the ions after the charge separation step.
The lengths of the small edges of the hexagon can be calculated as follows:

$$l_1 = \frac{{q_1}^{(1)}}{F} \tag{2.45}$$

and

$$l_2 = \frac{{q_2}^{(1)}}{F} \tag{2.46}$$

where with F it was denoted the electric force acting upon the ions in the spectrometer, while $q_1(1)$ and $q_2(1)$ are the kinetic momenta of B^+ and C^+.

The kinetic energy releases of the three steps are determined according to:

$$U_1 = \frac{p^2}{2\frac{m_{AB}m_{CD}}{m_{AB}+m_{CD}}} \tag{2.47}$$

$$U_2{}^{(1)} = \frac{{p_2}^{(1)2}}{2\frac{m_A m_B}{m_A+m_B}} \tag{2.48}$$

and

$$U_2{}^{(2)} = \frac{p_2{}^{(2)^2}}{2\frac{m_C m_D}{m_C+m_D}} \tag{2.49}$$

where $U_2{}^{(1)}$, $U_2{}^{(2)}$, $p_2{}^{(1)} = |\overrightarrow{q_2{}^{(1)}} - \overrightarrow{p}|$ and $p_2{}^{(2)} = |\overrightarrow{q_2{}^{(2)}} - \overrightarrow{p}|$ are the kinetic energy releases and the kinetic momenta corresponding to the loss of neutrals, respectively, whereas U_1 is the KER of the charge separation process.